Journal of Materials Chemistry A

ROYAL SOCIETY OF CHEMISTRY

PAPER

View Article Online
View Journal

Cite this: DOI: 10.1039/d5ta07705b

Electrophoretic fabrication of alcohol-stable $CsPbBr_3$ nanocrystalline photoelectrodes for formaldehyde production

Andrés F. Gualdrón-Reyes, *[ab] Camilo A. Mesa, *[a] Seul-Yi Lee,[ac] Roser Fernández-Climent, [ad] Sofia Masi, [a] Federica Aiello, [e] Federica Balzano, [f] Gloria Uccello-Barretta, [f] Ignacio Utreras-Asenjo,[b] Jeevan Torres,[a] Samiksha Mukesh Jain,[a] Carina Pareja-Rivera, [a] Hyo Joong Lee,[c] Jhonatan Rodríguez-Pereira, [gh] Sixto Giménez*[a] and Iván Mora-Seró *[a]

Beyond their established role in photovoltaics and optoelectronics, halide perovskites (HPs) are emerging as promising photoactive materials for solar-driven (photo)electrochemical (PEC) reactions, aimed at fuel and energy generation. However, their fast degradation in polar solvents severely affects their PEC redox performance, making protective coatings or the use of non-polar systems essential to preserve their structural integrity. Here, we report the fabrication of bulky quaternary ammonium-stabilized $CsPbBr_3$ perovskite nanocrystal (PNC) photoanodes *via* butanol (BuOH)- mediated electrophoretic deposition (ED), without any encapsulation, exhibiting high PEC performance in fully alcoholic environments. By carrying out the ED of PNCs in the presence of didodecyldimethylammonium bromide (DDAB) dissolved in BuOH, we modulate the PEC behavior of the films, obtaining an average photocurrent of 1.17 ± 0.19 mA cm^{-2} with a maximum value up to 1.45 mA cm^{-2} in methanol (MeOH) under visible light irradiation. We attribute this performance to a fine balance between DDAB-mediated surface defect passivation, limited alcohol permeation and efficient electron transport within the PNC active layer. These factors collectively result in a high oxidizing power, enabling the selective conversion of MeOH into formaldehyde, with a faradaic efficiency ~60% after 30 min of continuous operation. This work offers a novel and facile approach to fabricate high-quality PNC photoelectrodes with enhanced PEC activity for solar-driven chemical reactions in polar solvents.

Received 19th September 2025
Accepted 29th December 2025

DOI: 10.1039/d5ta07705b

rsc.li/materials-a

1 Introduction

The growing world energy demand, the contamination of ecosystems by industrial pollutants and the rising levels of greenhouse gas emissions, have driven the search for innovative alternatives to produce cleaner energy and remediate persistent wastewater pollutants. Among the promising processes is (photo)electrochemical (PEC) technology, which leverages photoactive semiconductors with exceptional light harvesting and carrier transfer/transport properties.[1,2] When a semiconductor-based photoelectrode is illuminated with photons, with equal or higher energy than its bandgap, photogenerated carriers are created and physically separated through an external bias.[3,4] Holes accumulate in the valence band (VB), while electrons are transferred through the conduction band (CB), enabling redox reactions at the semiconductor/electrolyte interface.[5]

In PEC systems the preparation of photoelectrodes plays a pivotal role, as it directly influences charge carrier dynamics and facilitates the extraction of electrons to be transported through the external circuit of the system. Different types of photoelectrodes have been developed for efficient PEC solar-driven applications based on metal oxides,[6–9] chalcogenides,[10,11] or carbonaceous materials[12–14] and their heterostructures.[15–17] However, several challenges need to be overcome, since (i) many semiconductors exhibit optimal performance under UV light,[18]

[a]Institute of Advanced Materials (INAM), Universitat Jaume I (UJI), Avenida de Vicent Sos Baynat, s/n, 12071 Castelló de la Plana, Castellón, Spain. E-mail: sjulia@uji.es; sero@uji.es

[b]Facultad de Ciencias, Instituto de Ciencias Químicas, Isla Teja, Universidad Austral de Chile, 5090000, Valdivia, Chile. E-mail: andres.gualdron@uach.cl

[c]Department of Chemistry and Research Institute of Physics & Chemistry, Jeonbuk National University, Jeonju 561-756, South Korea

[d]Department of Surface and Plasma Science, Faculty of Mathematics and Physics, Charles University, 180 00, Prague 8, Czech Republic

[e]National Research Council, Institute for Chemical and Physical Processes (CNR-IPCF), Via G. Moruzzi, 1, 56124, Pisa, Italy

[f]Department of Chemistry and Industrial Chemistry, University of Pisa, Via G. Moruzzi 13, 56124, Pisa, Italy

[g]Center of Materials and Nanotechnologies, Faculty of Chemical Technology, University of Pardubice, Nam. Cs. Legii 565, 53002 Pardubice, Czech Republic

[h]Central European Institute of Technology, Brno University of Technology, Purkyňova 123, 61200 Brno, Czech Republic

(ii) a fast recombination mechanism of the photogenerated carriers reduces their photoactivity[19,20] and (iii) poor stability leads to fast photodegradation under operational conditions.[21,22] Therefore, advancing PEC technology toward real-world applications requires the development of robust photoelectrodes with efficient light absorption and enhanced carrier transfer dynamics.

In the quest for synthesizing potential photoactive materials, halide perovskite nanocrystals (PNCs) have emerged as highly promising candidates to meet the key requirements for PEC applications. In addition to their ultrahigh photoluminescence quantum yield (PLQY), high extinction coefficient,[23] multi-exciton generation and efficient carrier transport properties,[24] PNCs are also attractive for their low-cost synthesis and facile processing methods,[25,26] and their tunable band structure and bandgap controlled through defect/composition engineering[27,28] and particle size variation.[29] For PEC reactions, this tunability enables the modulation of their VB and CB relative positions to favor oxidizing or reducing behavior.[30] We have correlated the PEC behavior of PNCs with their chemical composition particularly focusing on the halide species.[31] This knowledge has led to the development of PNC-based photocatalysts for the degradation of complex organic molecules including β-naphthol[30] and 2-mercaptobenzothiazole,[31] as well as the design and fabrication of photoanode/photocathode tandem arrangements for the selective oxidation/reduction of benzyl alcohol/benzaldehyde, respectively.[32] Furthermore, the use of PNCs in PEC H_2 production,[33] CO_2 reduction,[34] and PC polymerization[35] has been reported, often with high efficiencies. However, most of these studies have been performed in low-polarity solvents to preserve the structural integrity of PNCs, since these materials are prone to rapid degradation and loss of functionality in polar solvents.[36–38] Consequently, the application of PNC photoelectrodes in polar media remains underexplored in the current state of the art.

Several approaches have been proposed to improve the stability of PNCs in polar electrolyte solutions for PEC reactions. Common approaches involve material passivation with inorganic layers such as Ni_3P,[39] metal–organic frameworks,[40] or metal oxides (*e.g.* TiO_2 nanorods/nanotubes),[41] which help prevent direct interaction between PNCs and polar molecules, without obstructing light absorption required for photocarrier generation. Nevertheless, the eventual diffusion of H_2O and O_2 can decrease the PEC performance over time. More recently, the use of conductive carbon-based layers such as graphite, carbon black or combinations has been integrated to fabricate efficient $CsPbBr_3$ photoanodes, improving the electron extraction and injection from the electrode to the electrolyte solution to achieve photocurrents up to ~7–8 mA cm^{-2}. More importantly, these layers act as a protective coverage to extend the long-term stability of the photoactive material up to 168 h under continuous operation.[42–45] Alternatively, ligand passivation has been employed to fill/replace structural defects,[46,47] reducing non-radiative recombination traps,[48] and potentially improving charge transfer to the electrolyte.[49] Yet, the presence of long-chain organic ligands results in an insulating oily layer, that severely hinders carrier transport within the photoelectrode.[50] These limitations underscore the significant challenge of fabricating stable, efficient PNC-based photoanodes for operation in polar environments. Thus, innovative strategies to overcome these drawbacks, enhance PNC stability in polar solvents, and fabricate efficient PNC photoelectrodes with improved resistance under such environmental conditions are urgently needed.

We report for the first time the fabrication of $CsPbBr_3$ nanocrystalline photoanodes through electrophoretic deposition (ED), using didodecyldimethylammonium bromide (DDAB) dissolved in butanol (BuOH). This ligand acts as a protective layer against the full polar medium. As we previously demonstrated, PNC dispersions show long-term stability in alcohol-based solvents up to 10 months,[51] which facilitates the preparation of high-quality photoelectrodes with PLQY up to 72% in this study. By systematically analyzing the effect of DDAB concentration on the PEC performance of $CsPbBr_3$ PNC photoanodes immersed directly in different alcohol media, we identify 8.5 mM DDAB as the optimal condition. At this concentration, a favorable balance between effective passivation of defect sites through the incorporation of DDA^+, Br^- and alkoxide anions ($R–O^-$) from partial alcohol ionization and controlled permeation of alcohol molecules to the PNC/electrolyte interface is achieved. Furthermore, carrier separation and transport through the PEC cell is facilitated, improving electron injection towards the photoanode during alcohol oxidation, exhibiting a photocurrent of 1.45 mA cm^{-2} in the absence of any encapsulation. This work demonstrates the feasibility of using DDAB-capped PNC photoanodes for triggering efficient PEC organic transformation in polar environments, opening new opportunities for solar-PEC reactions with halide perovskite materials.

2 Results and discussion

As-prepared green-emitting $CsPbBr_3$ PNCs were dispersed in DDAB/BuOH solutions (hereafter referred to as PNCs-BuOH), with varying concentration of the quaternary alkylammonium bromide (AlkylBr) ligand set at 0, 4.3, 8.5, 17, 43 and 85 mM; see the SI for details. Transmission electron microscopy (TEM) images of the resulting PNCs-BuOH dispersions show monodisperse nanocubes with an average particle size between 8 and 10 nm, see Fig. S1A–F, with a narrow size distribution, see Fig. S2A–F, indicating good size homogeneity of the PNCs after DDAB addition. The $CsPbBr_3$ PNC active layers were then fabricated by ED, by immersing a FTO substrate with a compact/mesoporous TiO_2 film (TiO_2/FTO) into PNCs-BuOH dispersions, using a two-electrode cell configuration under an applied bias of 250 V, see Fig. 1A. Under these conditions, DDAB-capped PNCs-BuOH were deposited on the cathode, exhibiting intense luminescence, while the pristine (uncapped) PNCs were deposited on the anode, displaying weaker emission, see Fig. 1A′. In both cases, TiO_2/FTO electrodes served as the anode and the cathode. The different migration behavior between capped and uncapped PNCs suggests a significant surface charge modification induced by DDAB passivation. Specifically, pristine PNCs show a negative surface charge, attributed to the

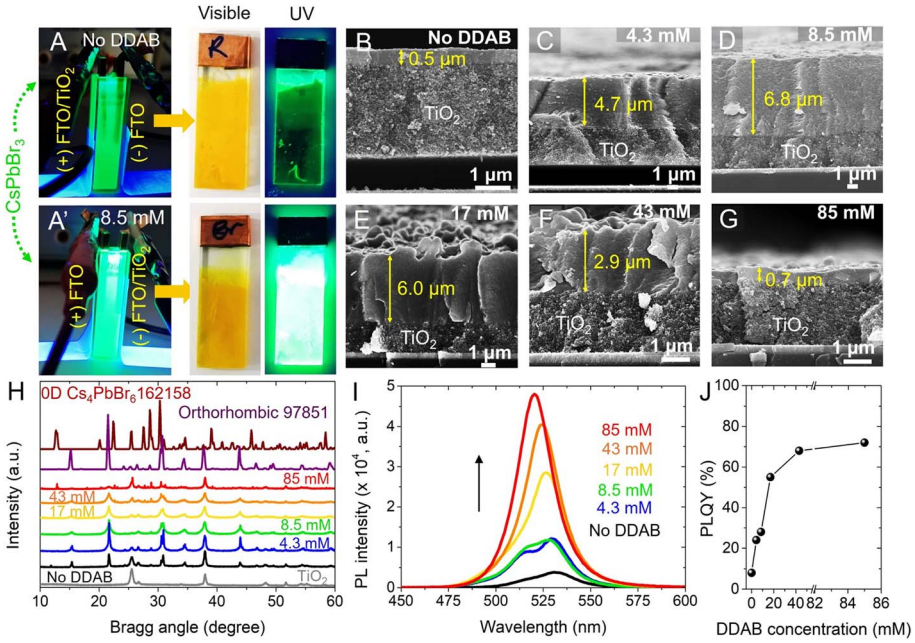

Fig. 1 Electrophoretic deposition of green-emitting $CsPbBr_3$ PNCs on a FTO/TiO_2 electrode (A) in the absence and (A′) presence of 8.5 mM DDAB in a BuOH solution, at 250 V for 60 s. Cross-sectional SEM images of FTO/TiO_2/$CsPbBr_3$ PNC photoelectrodes in (B) the absence and with different DDAB concentrations: (C) 4.3 mM, (D) 8.5 mM, (E) 17 mM, (F) and (G) 85 mM. Yellow arrows indicate the thickness of $CsPbBr_3$ layers. (H) XRD patterns, (I) PL spectra and (J) PLQY measurements of photoelectrodes with and without DDAB.

chemical surface environment containing halide and oleate anions, while DDAB-capped PNCs exhibit a positive charge, due to the exposure of DDA^+ species in the polar BuOH solvent.

To examine the surface morphology of pristine and DDAB-capped PNC photoelectrodes after the ED process, Scanning Electron Microscopy (SEM) was performed. Top view images of the PNC films (Fig. S3A–F) show nanoparticle agglomeration, irrespective of DDAB concentration. This aggregation is attributed to the field-driven diffusion of PNCs toward the TiO_2/FTO electrode during deposition, which promotes partial coalescence of the nanocrystals.[52] Cross-sectional SEM images were also obtained to elucidate how the amount of DDAB linked to the PNC surface influences the thickness of deposited films, see Fig. 1B–G. Average thicknesses of TiO_2 and PNC layers constituting the respective photoelectrodes are shown in Table S1. Up to a concentration of 8.5 mM, the film thickness increases, reaching a maximum value of 6.8 ± 0.1 μm. However, at higher concentrations, the film becomes progressively thinner. This suggests that an optimal DDAB concentration (8.5 mM) imparts sufficiently positive surface charge to the PNCs, enhancing their electrophoretic mobility and facilitating the deposition onto the TiO_2/FTO substrate. Beyond this concentration, excessive ligand coverages likely cause steric hindrance and surface insulation, reducing particle mobility and resulting in thinner films. Achieving the right balance between effective ligand passivation and adequate film formation is critical to ensuring efficient carrier separation and transport through the PEC cell, as we will discuss below.

To investigate the crystalline structure of PNC photoelectrodes in the presence of the DDAB ligand, X-ray diffraction (XRD) measurements were carried out on the as-prepared materials. As shown in Fig. 1H, all samples exhibit the typical XRD profile of the orthorhombic phase (ICSD 97851).[53] Nevertheless, by increasing the DDAB concentration (particularly at 85 mM), a clear reduction in the intensity of the $CsPbBr_3$ peak is observed, together with the appearance of new signals ascribed to the 0D Cs_4PbBr_6 (ICSD 162158).[54] This behavior is attributed to the 3D-to-0D structural reorganization, likely caused by the exfoliation of $[PbBr_6]^{4-}$ octahedra from the $CsPbBr_3$ lattice due to interaction with the AlkylBr ligand. The formation of Cs_4PbBr_6 can also enhance the optical features of the PNC photoelectrodes, since this 0D perovskite can serve as a protective passivating shell effectively suppressing non-radiative recombination channels and contributing to improved photocarrier dynamics.[55]

The optical properties of PNC photoelectrodes were significantly influenced by the DDAB concentration, see Fig. 1I. For the sample without DDAB and those with low ligand concentrations, the photoluminescence (PL) spectra display broad emission with a noticeable double peak feature. In contrast, at higher ligand concentrations, this feature disappears, and the PL peak exhibits a clear blue shift, which aligns well with the corresponding obtained absorption spectra, see Fig. S4A. This behavior is attributed to the differences in particle size distribution: the no DDAB sample shows a broader distribution, while increasing ligand concentration results in a narrower and more uniform size distribution, see Fig. S2. We propose that higher DDAB concentrations provide a higher density of the AlkylBr ligand that rapidly caps the PNCs,[56] leading to more homogeneous particle formation. Then, the PL quantum yield

(PLQY) of the photoanodes is progressively improved at higher DDAB concentrations, see Fig. 1J, inferring that DDAB also favors an effective ligand passivation in the perovskite surface, filling/replacing Cs^+ and Br^- defect sites.[51] At this point, the nonradiative recombination mechanism is suppressed, enhancing the PL properties of the photoactive material.[57] Simultaneously, carrier separation is also promoted by the TiO_2 electron transport layer in the photoelectrodes, see Fig. S4B, leading to a lower PL intensity compared to the photoactive material without the TiO_2 layer. This creates an ideal scenario for efficient electron extraction and transport in the photoelectrode, triggering the PEC alcohol oxidation, as we will discuss later. Lastly, to obtain information about the light-harvesting capability of the samples, we have calculated the absorption coefficient, α, for the photoactive material in the presence of 8.5 mM DDAB by using the equation: $\alpha = 2.303\left(\frac{A}{L}\right)$, where A and L are the absorbance and thickness (cm) of the photoactive layer, respectively. In this context, considering that $A = 1.66$ and $L = 6.8 \times 10^{-4}$ cm, we estimated $\alpha = 5.62 \times 10^3$ cm^{-1}, this value being realistic for $CsPbBr_3$ films near their absorption onset.[58]

Regarding stability, pristine PNCs lose nearly all PL emission after 15 days of exposure to ambient air, while DDAB-capped PNCs (8.5 mM), retain most of their emission, with only a slight decrease, see Fig. S4C and C′. To further assess recombination dynamics, time-resolved PL measurements were conducted on the DDAB-capped $CsPbBr_3$ photoelectrodes, see Fig. S4D. The PL decay profiles fit well to a bi-exponential model, where the long-lived component is ascribed to optical effects, such as light scattering from the solid, resulting in a more efficient reabsorption/re-emission process,[59] which can extend the apparent decay time. At this point, we focused on the shorter lifetime component to analyze the intrinsic recombination dynamics. These lifetimes were estimated as 4.95, 6.38 14.68 and 13.05 ns for pristine PNCs and samples with 8.5 mM, 17 mM and 85 mM DDAB, respectively. Accordingly, the higher the PLQY, the longer the lifetime at higher DDAB concentrations, confirming that increased ligand concentration effectively passivates surface defects and suppresses non-radiative recombination pathways.

The influence of DDAB concentration on the surface chemistry of PNC photoelectrodes was further investigated through X-ray Photoelectron Spectroscopy (XPS), see Fig. S5. The survey spectra confirmed the presence of key elements such as C, O, N, Cs, Pb, and Br, with their relative compositions summarized in Table S2. High-resolution (HR) XPS spectra were then analyzed to get insights into the chemical speciation of each element. Fig. S6A exhibits the HR-XPS Cs 3d spectra of the DDAB-capped PNC electrodes, displaying the typical $3d_{5/2}$ and $3d_{3/2}$ signals at ~724/738 eV, ascribed to Cs^+ ions within the perovskite lattice.[60] Similarly, HR-XPS Pb 4f spectra (Fig. S6B) show the characteristic $4f_{7/2}/4f_{5/2}$ doublet at ~138/143 eV, indicative of Pb^{2+} ions forming part of the $[PbBr_6]^{4-}$ octahedra. The formation of Pb–Br bonds in the perovskite lattice is further supported by the HR-XPS Br 3d spectra (see Fig. S6C), depicting the $3d_{5/2}/3d_{3/2}$ doublet at ~68/69 eV, consistent with Br^- in the perovskite structure.[61] Lastly, the HR-XPS N 1s spectra (Fig. S6D) exhibit a single signal at ~402 eV, corresponding to the alkylammonium species ($R–NH_3^+$) surrounding the PNC surface.[62]

XPS analysis further reveals that in the absence of DDAB modification, the pristine photoelectrode shows a noticeable Cs^+ deficiency, see Fig. 2A, indicating the emergence of defect sites, consistent with the deterioration of its optical properties. This is expected due to the low binding affinity of OA/OLA to the perovskite surface,[63] which leaves the material vulnerable in polar environments. Upon DDAB addition, the Cs^+ deficiency is progressively mitigated, improving the Cs/Pb stoichiometry toward ~1.0. However, the Br^- content is slightly reduced (particularly at the 8.5–43 mM DDAB range) compared to the pristine sample, see Fig. 2A.

Simultaneously, the $C–NH_3^+$ fraction in the surface increases with rising AlkylBr concentration, see Fig. 2B. This observation helps to explain the changes in surface charge of the PNCs after electrophoretic deposition. In the pristine sample, the presence of Cs^+ vacancies results in a greater surface exposure of Br^- ions, contributing to a negative surface charge that promotes the diffusion to the anode. In contrast, raising the DDAB concentration enriches the surface of the PNC with DDA^+

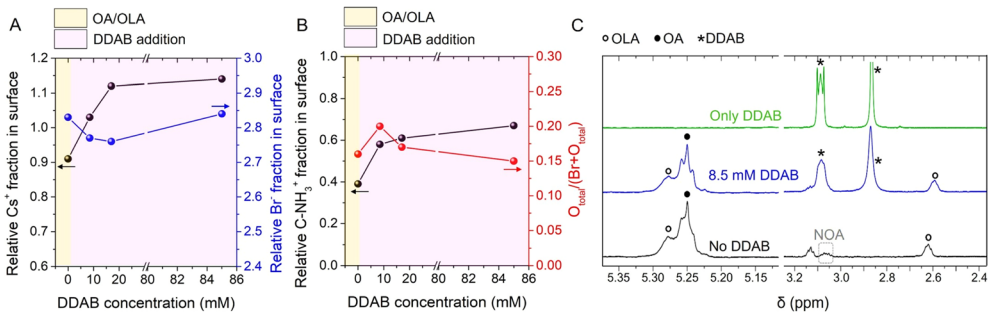

Fig. 2 Relative fractions in the surface as determined by XPS analysis: (A) Cs^+ and Br^- fractions and (B) $C–NH_3^+$ and $O_{total}/(Br + O_{total})$ ratios for $CsPbBr_3$ photoelectrodes in the absence and presence of DDAB. (C) ^1H (600 MHz, butanol-d_{10}/toluene-d_8 2 : 1 v/v, 298 K) NMR spectra of $CsPbBr_3$ PNCs in the absence (black spectrum) and presence of 8.5 mM DDAB (blue spectrum), with expansion of the olefinic region (5.35–5.10 ppm) and of the methylene region (3.25–2.40 ppm). Characteristic NMR resonances of DDAB in the absence of perovskite were also reported for comparison (green spectrum).

species, shifting the surface charge to positive and driving deposition onto the cathode. This suggests that Br^- ions are less exposed to the surface, indicating effective surface passivation by the alkylammonium cations.

Finally, analysis of the total oxygen-to-bromide ratio (denoted as $[O_{total}/(Br + O_{total})]$ across the photoelectrodes), see Fig. 2B, reveals that the 8.5 mM DDAB sample shows the highest ratio. This suggests that butanol-derived butoxide anions (BuO^-), formed *via* partial ionization during OLA^+/DDA^+ exchange help compensate Br^- deficiencies, contributing to the material stabilization.[64] However, at higher DDAB concentrations, the oxygen content decreases, indicating that DDA^+ species increasingly inhibit BuOH permeation into the PNC core. Interestingly, this trend is similar to the observed variation in film thickness, see Fig. 1B–G, supporting that 8.5 mM DDAB represents the optimal condition. Beyond this value, excess DDAB impedes both the PNC migration toward the TiO_2/FTO electrode, and interaction with alcohol species.

To analyze the interaction at molecular level between DDAB and PNCs during the photoelectrode fabrication, Nuclear Magnetic Resonance (NMR) measurements were conducted. The analysis aimed to identify the NMR signals of surface ligands bound to $CsPbBr_3$ PNCs, both in the presence and absence of 8.5 mM DDAB.[64] In the ^1H NMR spectrum of PNCs, characteristic resonances at $\delta = 5.30$–5.25 ppm and 2.62 ppm are assigned to the olefinic protons of OLA and OA chains, and to the methylene in the α-position of the amino group of OLA, respectively, see Fig. 2C. OA/OLA interaction also mediates the formation of *N*-oleyloleamide (NOA), confirmed by its typical signal at $\delta = 3.06$ ppm, ascribed to methylene linked to the amide moiety. In the presence of DDAB, besides the signals of capping ligands, characteristic resonances at $\delta = 3.09$ and 2.87 ppm (Fig. 2C) are attributed to methylene and methyl moieties linked to the ammonium group of DDAB, respectively.

Compared with previous data acquired for PNCs in pure toluene in the absence of DDAB,[64] OA/OLA signals display narrower linewidths in the butanol/toluene mixture. This evidence suggests a weaker interaction between the capping ligands (OLA/OA) and the PNC surface in the presence of a polar co-solvent, implying a more labile ligand shell under these conditions. A similar trend is observed in DDAB/PNCs mixture for both capping ligands and additive resonances, which appear significantly broadened in toluene. This result suggests stronger interactions in the absence of the polar solvent even in the presence of DDAB. In butanol/toluene, such interactions are moderated by the increased polarity and protic nature of the solvent mixture, likely due to competitive hydrogen bonding effects. Interestingly, despite the weaker DDAB/PNCs interaction in butanol/toluene, the overall stability of PNCs is significantly enhanced: while the PNCs without the additive exhibit visible precipitation within 16 h, the presence of DDAB stabilizes the solution, which remains clear over the same period. This result indicates the favorable protective effect provided by DDAB (linked to the material surface *via* DDA^+ and Br^- ions) against the alcohol medium, keeping the OA/OLA interactions with the perovskite.

Additionally, the presence of DDAB in butanol/toluene is responsible for a shielding of the OLA resonance at 2.62 ppm (Fig. 2C), as opposed to the simple mixture of DDAB and capping ligands, see Fig. S7, where a deshielding of the same resonance is found. Therefore, this shielding effect indicates a partial ligand exchange between DDA^+ and OLA^+ species, which is beneficial for the subsequent alcohol ionization as we have previously reported.[64] This interplay of ligand exchange and alcohol ionization is crucial for understanding the behavior of PNC systems: in the presence of DDAB, the less polar nature of butanol, relative to shorter-chain alcohols such as methanol, makes it less effective in weakening the OA/OLA coordination shell, thus providing a chemical environment that favors PNC stabilization. Taken together, the NMR results reinforce the hypothesis that, in the presence of polar solvents, DDAB plays a strategic role in tuning the strength and the dynamics of ligand–surface interactions and stabilizing the PNC surface. This chemical behavior could be considered a key parameter in the rational design of future systems.

To identify optimal conditions for fabricating efficient $CsPbBr_3$ nanoparticle-based photoelectrodes with enhanced PEC performance, we systematically investigated the effects of ED time, the number of mesoporous TiO_2 layers, and the concentrations of both PNCs and DDAB on the photoresponse of the electrodes. For this purpose, chopped-light voltammetry measurements were carried out to evaluate the PEC performance of the photoanodes. These tests were conducted in pure BuOH, containing 45 mM methylammonium bromide (MeBr) as the supporting electrolyte, under several visible light on/off cycles, without any encapsulation.

As a starting point, we examined the influence of ED time of PNCs on top of one mesoporous TiO_2 (*m*-TiO_2) layer (deposited on a FTO substrate through the doctor blade method), while keeping the DDAB concentration fixed at 85 mM and varying the PNC concentration. As shown in Fig. S8A, increasing the ED time up to 60 s at 15 mM PNCs led to a gradual rise in anodic photocurrent, suggesting improved nanoparticle loading and enhanced photocarrier generation, with electron transport through the PEC cell. Then, a longer ED time promotes the appearance of some cracks on the photoelectrode surface, often producing the detachment of the PNC active layer. On the other hand, when comparing the photoresponse of pristine and DDAB-capped $CsPbBr_3$ photoanodes, both fabricated under the same ED time (60 s), a higher photocurrent is observed with the modified photoactive material, which can be explained by a more uniform surface, mediating an adequate particle-to-particle interconnection for the carrier transport. In contrast, the emergence of a high density of nanoparticle aggregates in the pristine perovskite photoanode can restrain the electron extraction and mobility (electron trapping), decreasing the performance of the PEC cell. However, the maximum photocurrent achieved, $\sim$60 $\mu A\ cm^{-2}$, remained relatively low compared to current benchmarks, indicating that further enhancement required higher PNC loading. Subsequently, increasing the PNC concentration to 30 mM, see Fig. S8B, led to a notable 5-fold increase in photocurrent. This enhancement is attributed to improved interparticle electron mobility and more

efficient extraction which in turn facilitates hole accumulation at the material/electrolyte interface, promoting oxidation reactions. Under these conditions, a maximum photocurrent of ~0.25 mA cm^{-2} was obtained at applied potentials ≥0.2 V *vs.* Ag/Ag^+, see Fig. S8C. Conversely, further increasing the PNC concentration to 50 mM led to a decline of the photocurrent, likely due to hindered electron transport and extraction from the photoactive material, see Fig. S8D, orange curve. In this scenario, excessive nanoparticle loading increases the density of grain boundaries, which promotes carrier recombination *via* electron trapping.

A similar behavior was achieved when increasing the number of layers (up to 3), using both 30 mM and 50 mM PNCs, (Fig. S8D–F), detailing that using 1 *m*-TiO_2 layer is enough to promote an efficient PEC performance. In this way, thicker TiO_2 layers impose longer transport distances for electrons before reaching the extracting contact, which increases the probability of recombination and reduces photocurrent. Additionally, excessive transport resistance within the denser matrix may further obstruct carrier mobility throughout the PEC system.[65] Notably, in all cases, the photocurrent remained stable along the light on/off cycles. This behavior highlights the effective ligand passivation provided by DDAB, which protects the perovskite surface from degradation in the BuOH medium. Next, we aimed to optimize the PEC performance of $CsPbBr_3$ photoanodes by modulating the DDAB concentration during the ED process and by testing diverse alcohols as hole scavengers to trigger oxidation reactions. To this end, chopped light-voltammetry measurements (7 light on/off cycles) were conducted to evaluate the photoresponse and stability of the photoanodes as a function of both DDAB concentration and the nature of alcohol.

$CsPbBr_3$ photoelectrodes were individually immersed in four different alcohols, namely methanol (MeOH), ethanol (EtOH), 1-propanol (1-PrOH) and 1-butanol (1-BuOH), varying the DDAB concentration (0, 4.3, 8.5, 17, 43 and 85 mM). As shown in Fig. 3A–D, the photocurrent exhibited a clear dependence on DDAB concentration, with the highest photoresponse consistently observed at 8.5 mM in all alcohol environments. To assess the reproducibility of the results at this optimal concentration, 3 independent photoanodes were measured in each alcohol medium, with the maximum photocurrent values shown in Fig. S9A–D. Among the alcohols tested, MeOH yielded the highest average response (~1.12 ± 0.12 mA cm^{-2} at 0.1 V *vs.* Ag/Ag^+) with the best sample reaching ~1.24 mA cm^{-2}, see Fig. 3E. For DDAB concentrations above 8.5 mM, the PEC performance declined, likely due to excessive ligand coverage, forming an insulator layer, which blocks the mobility of alcohol molecules to the PNC surface.

Additionally, the nature of the alcohol significantly influenced the PEC response. Specifically, shorter-chain alcohols produced higher photocurrents, which was attributed to the higher permeability and ease of access to the perovskite core, promoting electron injection. In contrast, bulkier alcohol molecules, such as BuOH, interact less efficiently with the PNCs, due to steric hindrance, which can induce surface distortions and limit reaction efficiency.[64] Accordingly, the shorter-chain alcohols are more likely to diffuse towards the photoelectrode/electrolyte interface, increasing their oxidation kinetics, see Fig. 3F.

After evaluating the PEC performance of multiple $CsPbBr_3$ photoelectrodes (5 additional samples) containing 8.5 mM DDAB and using MeOH as a hole scavenger under ≥12 light on/off cycles, see Fig. S10A and B, the average maximum

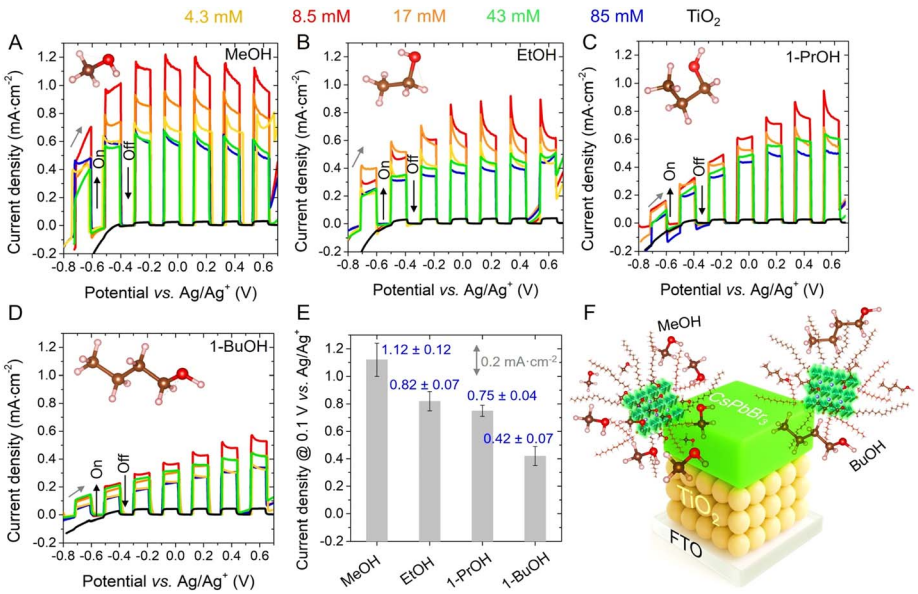

Fig. 3 Chopped light linear sweep voltammetry measurements showing the photocurrents of TiO_2 and $CsPbBr_3$ photoanodes by varying the DDAB concentration under visible light illumination (100 mW cm^{-2}, UV filter) in 45 mM MeBr in different alcohol electrolytes: (A) MeOH, (B) EtOH, (C) 1-PrOH and (D) 1-BuOH. (E) Average photocurrents (with error bars from 3 diverse samples) of $CsPbBr_3$ photoanodes modified with 8.5 mM in the different alcohol electrolytes at 0.1 V *vs.* Ag/Ag^+. (F) Schematic representation of a high density of the small MeOH species reaching the photoanode surface, compared to the low density of the long BuOH species.

photocurrent was estimated to be 1.17 ± 0.19 mA cm^{-2} in the potential range of −0.24 to −0.17 *vs.* Ag/Ag^+, and 0.98 ± 0.11 mA cm^{-2} in the range of 0.08 to 0.18 *vs.* Ag/Ag^+, see Fig. S10C. The best performing photoelectrode achieved a peak photocurrent of ∼1.45 mA cm^{-2} at −0.17 V s *vs.* Ag/Ag^+. To the best of our knowledge, this is the highest reported value for a perovskite-based photoelectrode operating in direct contact with a polar solvent under visible light, without any encapsulation. The photocurrent was also found to be more reproducible under anodic potentials. These results confirm that the addition of 8.5 mM DDAB provides an optimal balance between nanoparticle content and surface passivation, enabling efficient electron injection during alcohol oxidation and resulting in highly stable PEC performance. Finally, although using a 1 *m*-TiO_2 layer leads to the highest PEC activity in the photoanodes, an average thickness of ∼3 μm (as estimated from cross-sectional SEM) is likely still excessive for maximizing carrier separation and extraction from the $CsPbBr_3$ PNC layer. Therefore, thinner *m*-TiO_2 layers prepared by alternative approaches such as spray-pyrolysis and chemical bath deposition are expected to provide a more favorable compromise between the light harvesting and electron mobility within the photoanode, enhancing the photoresponse of the PEC cells.

Then, to observe the influence of DDAB on the interfacial carrier resistance and accumulation of $CsPbBr_3$ photoanodes into the MeOH environment, electrochemical impedance spectroscopy (EIS) measurements were conducted in the photoactive materials in the presence and absence of the AlkylBr ligand under constant visible light at 0.1 V *vs.* Ag/Ag^+. Here, a Randles-type equivalent circuit was used to model the corresponding Nyquist plots, see Fig. S11, to determine the series resistance (R_s), interfacial carrier transport resistance (R_{ct}) and double-layer capacitance (C_{dl}) values, summarized in Table S3. A higher R_{ct} is noted for the DDAB-capped photoanode compared with the pristine perovskite, which corroborates the protective effect of DDAB, restraining the diffusion of a high density of MeOH molecules to reach the PNC core. Conversely, a lower R_{ct} in the pristine material is an indication of the faster migration of MeOH towards PNCs in the photoanode/electrolyte interface, causing their eventual deterioration. Simultaneously, an approximately twofold decrease in C_{dl} is observed for the DDAB-capped $CsPbBr_3$ photoanode relative to the pristine material, indicating more efficient carrier extraction and transport. This effect arises from effective surface passivation of Cs^+ and Br^- defect sites, which mitigates carrier trapping.

Building on the successful surface modification strategy applied to $CsPbBr_3$, we extended this approach to stabilize red-emitting DDAB-capped $CsPbI_3$ PNC based photoanodes, by adding a low concentration of DDAB (8.5 mM), as shown in Fig. S12A. This ligand concentration effectively passivated the surface of iodide-based PNCs. As shown in Fig. S12B, the prepared $CsPbI_3$ photoanode remains stable after 15 days under ambient air, exhibiting an increase in PL intensity. This enhancement, together with a blueshift in the PL emission suggests that the Br^- species from the DDAB ligand can gradually compensate iodide vacancies contributing to improved surface passivation. Despite this apparent stabilization, the photoelectrochemical (PEC) activity of the $CsPbI_3$-based photoanode (tested in 45 mM MeBr/MeOH) shows a maximum photoresponse of ∼0.30 mA cm^{-2}, which is notably lower than that of its $CsPbBr_3$ counterpart. Moreover, this photocurrent decreases faster, see Fig. S12C, indicating that DDAB does not sufficiently suppress the migration of iodide ions,[66] leading to faster material degradation and loss of PEC performance. Nevertheless, these results provide a promising starting point to develop ligand engineering strategies tailored to different halide compositions. In this context, the use of passivating ligands such as DDAB may offer a viable pathway for improving the stability and electrochemical functionality of various $CsPbX_3$ (X = Cl, Br, I) nanocrystals in polar solvents, paving the way for their broader application in photoelectrochemical systems.

To evaluate the PEC power of DDAB-capped $CsPbBr_3$ photoanodes (using 8.5 mM DDAB), the PEC MeOH oxidation was performed. Although MeOH can easily permeate the DDAB coverage to react in the PNCs/electrolyte interface (as seen above), this alcohol also has a high polarity, which is pivotal for analyzing the stability of the photoactive material. In this context, the photoanode was immersed in pure MeOH in the presence of 45 mM MeBr, and operated under chopped illumination at 0.1 V *vs.* Ag/Ag^+ for 30 min. As shown in Fig. 4A, the system retained a stable photocurrent of ∼1 mA cm^{-2}. Over time, however, the photocurrent gradually decreased (Fig. 4B), suggesting: (i) mass-transfer limitations due to the high concentration of MeOH molecules reacting on the PNC surface and/or (ii) the progressive degradation of the perovskite under operational conditions.

To investigate the products formed during MeOH oxidation, a spectrophotometric titration was carried out using 4-amino-5-hydrazino-1,2,4-triazole-3-thiol in the presence of 1 M NaOH aqueous solution. The resulting violet color of the solution confirmed the formation of CH_2O with a faradaic efficiency (FE) ∼60%, see Fig. S13 and the SI for experimental details. The proposed oxidation mechanism is illustrated in Fig. 4C. Based on the band diagram of the FTO/TiO_2/$CsPbBr_3$ photoanode and the redox potential of the MeOH/CH_2O system, see Fig. S14, the following sequence is presented: a MeOH molecule reacts with the OLA species released after ligand exchange with DDAB, inducing the partial alcohol ionization to produce methoxide anions (MeO^-, eqn (1)):

$$C_{18}–NH_2 + CH_3OH \rightarrow C_{18}–NH_3^+ + CH_3O^- \quad (1)$$

Then, MeO^- species are adsorbed on the $CsPbBr_3$ photoanode (named $CH_3O_{ads}^-$) for compensating surface halide defects and facilitating the perovskite stabilization.[51,64] Then, after illuminating the photoanode, and photogenerating electron/hole pairs, holes accumulated in the VB migrate to the photoactive material surface (h_s^+), reacting with $CH_3O_{ads}^-$ to trigger the C–H acidic dissociation (inducing the release of a H^+) and concomitant formaldehyde formation (eqn (2)):

$$CH_3O_{ads}^- + h_s^+ \rightarrow CH_2O + H^+ + e^- \quad (2)$$

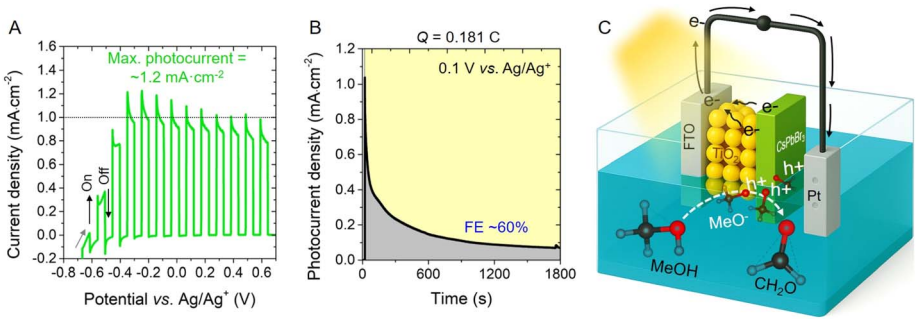

Fig. 4 (A) Chopped-light linear sweep voltammetry showing stable photocurrent from a $CsPbBr_3$ photoanode in the presence of 8.5 mM DDAB and (B) its corresponding chronoamperometry profile during photoelectrolysis by applying a bias of 0.1 V *vs.* Ag/Ag^+ for 1800 s. Experimental conditions: visible light illumination (100 mW cm^{-2}, UV filter) in 45 mM MeBr in MeOH. (C) Schematic representation of the PEC MeOH-to-CH_2O oxidation using the DDAB-capped $CsPbBr_3$ photoanode.

During the oxidation, electrons are extracted from the photoanode, being transported to the external circuit of the system, reaching the counter electrode. Here, oxygen reduction could be promoted in the presence of the formed H^+, producing H_2O molecules during the process (eqn (3)):[67]

$$\frac{3}{2}O_2 + 6H^+ + 6e^- \rightarrow 3H_2O \quad (3)$$

Alternative reaction pathways for MeOH oxidation reported in the literature consider the formation of intermediate species such as the methoxy radicals ($CH_3O^\bullet$), which are known to mediate the photocurrent doubling effect. Here, a secondary oxidation step is promoted *via* electron injection from the $CH_3O^\bullet$ species to the CB of the photoanode, increasing its photoresponse ~2-fold.[68] In this context, although we were not able to detect directly the emergence of $CH_3O^\bullet$ radicals during the PEC reaction, we proceeded to study their possible generation by conducting chopped-light voltammetry measurements by varying the amount of available MeOH molecules for the oxidation process. For this, we halved the MeOH content in the electrolyte solution, replacing it with deionized water (MeOH : H_2O volume ratio 1 : 1) and then we analyzed the PEC activity of a $CsPbBr_3$ photoanode in the presence of 8.5 mM DDAB in this prepared environment, observing more than 2-fold decrease in the photocurrent, see Fig. S15A. Thus, although the MeOH content is doubled to increase the PEC performance, the photocurrent doubling is not induced. This allows us to suggest indirectly that $CH_3O^\bullet$ radicals are not produced in our PEC system, with the MeOH-to-formaldehyde conversion mediated by the direct reaction of adsorbed MeO^- anions with the surface holes accumulated in the photoanode, being the most probable reaction pathway. On the other hand, to rationalize the uncounted 40% FE, taking into account the highly oxidizing VBM of the $CsPbBr_3$ photoanodes (1.36 V *vs.* Ag/Ag^+, see Fig. S14), we infer that these photoactive materials can oxidize MeOH to produce CO_2 and H_2 (~−0.14 V *vs.* Ag/Ag^+)[69] in the presence of H_2O produced during oxygen reduction, in accordance with the following reaction (eqn (4)):[70]

$$CH_3OH + 6h_s^+ + H_2O \rightarrow CO_2 + 6H^+ + 6e^- \quad (4)$$

Furthermore, h_s^+ would be also consumed by water molecules, favoring the water splitting reaction in the photoanode/electrolyte surface (~0.69 V *vs.* Ag/Ag^+, eqn (5)):

$$2H_2O + 4h_s^+ \rightarrow O_2 + 4H^+ + 4e^- \quad (5)$$

Considering the redox potentials for CO_2 formation and H_2O oxidation, the occurrence of the abovementioned reactions in parallel with CH_2O production is feasible, which could explain the consumption of the remaining current produced by the perovskite photoanode, associated with the unaccounted 40% FE.

Lastly, with the aim to observe the stability of the $CsPbBr_3$ photoanode in the presence of 8.5 mM DDAB in the full MeOH medium for a longer time, a chronoamperometric profile was obtained at 0.1 V *vs.* Ag/Ag^+, see Fig. S15B, demonstrating that the DDAB ligand provides a moderate operational durability for 1 h in the absence of any external protective layer or encapsulation. Here, further optimization of main parameters, including the applied voltage during the ED process and the TiO_2 annealing temperature will be studied, aiming at improved carrier separation/extraction and thereby, a stable photocurrent, enhancing the long-term PEC activity of the resulting photoanode. In conclusion, this study demonstrates that the combination of the ED process with surface engineering, using the DDAB ligand, enables the fabrication of $CsPbBr_3$ photoelectrodes, capable of driving redox transformations in fully polar environments. This approach offers a promising platform for converting solar energy into value-added chemical products *via* controlled PEC processes.

3 Summary and conclusions

In this work, we present a novel approach combining alcohol-mediated ED and ligand passivation for the fabrication of $CsPbBr_3$ PNC-based photoelectrodes with enhanced optical performance and tunable PEC activity for efficient alcohol oxidation in fully polar environments. The introduction of the DDAB ligand during the ED process modulates the surface charge of the deposited nanoparticles, simultaneously compensating surface defects and forming a protective DDA^+-rich layer that shields the perovskite

from solvent degradation. This strategy leads to a progressive enhancement of PL properties and a PLQY increase up to 72%, with increasing DDAB concentration. We systematically analyzed the influence of the alcohol structure and DDAB concentration on the PEC performance of the photoanodes. It was found that bulky alcohols, such as BuOH, are sterically hindered from accessing the perovskite surface, slowing charge transfer and suppressing photoactivity. In contrast, smaller alcohols such as MeOH can more readily reach the perovskite interface, facilitating efficient electron transfer and transport through the photoactive material.

An optimal DDAB concentration of 8.5 mM was identified, providing a balance between nanoparticle loading, defect passivation and charge carrier dynamics through the PEC cell. Under these conditions, the photoanode achieved a maximum photocurrent of 1.45 mA cm^{-2}, representing the highest reported photoresponse for a perovskite electrode operating in a polar environment without encapsulation. Moreover, bulk photoelectrolysis demonstrated the successful conversion of MeOH to CH_2O, with FE ~60%, highlighting the redox capability of $CsPbBr_3$ nanoparticles for photon-to-chemical energy conversion. This study provides a promising strategy for developing ligand-engineered halide perovskite photoelectrodes capable of functioning in polar solvents, opening the door to future applications in solar-driven PEC transformations. The presented approach can be further extended through additional interface engineering, such as protective coatings, to enable the development of robust and scalable photochemical platforms based on perovskite nanomaterials.

Author contributions

A. F. G.-R., C. M., S. G. and I. M.-S. conceived the project. A. F. G.-R., R. F.-C., S. G. and C. A. M. designed the experiments. A. F. G.-R., S.-Y. L., I. U.-A., J. T. and C. P.-R. synthesized PNC colloidal solutions and photoelectrodes, and performed the studies on corresponding morphological, structural, and optical properties. J. R.-P. contributed to the XPS measurements and analysis. S. M., F. A., F. B., and G. U.-B. designed and performed the NMR analysis. A. F. G.-R., C. A. M. and S. M. J. performed the photoelectrochemical measurements. A. F. G.-R. and C. A. M. coordinated the experimental work. A. F. G.-R. C. M., S. G. and I. M.-S. coordinated the whole project. All authors contributed to the discussions and the writing of the manuscript.

Conflicts of interest

The authors declare no conflicts of interest.

Data availability

Data for this article are available at Zenodo repository at web page: https://zenodo.org/uploads/18172665, with https://doi.org/10.5281/zenodo.18172665. Supplementary information: experimental setup, morphology, histograms, optical properties, XPS spectra, surface chemical composition, ^{1}H NMR spectra and photoelectrochemical measurements of DDAB-capped $CsPbBr_3$ photoelectrodes, and quantification of MeOH-to-CH_2O transformation by using the perovskite photoelectrodes by using 8.5 mM DDAB, scheme of band structure of the composite photoanode for redox reaction. See DOI: https://doi.org/10.1039/d5ta07705b.

Acknowledgements

This work was supported by the European Innovation Council (EIC) *via* the OHPERA project (grant agreement 101071010), the Ministry of Science and Innovation of Spain MCIN/AEI/10.13039/501100011033/ and by FEDER, UE under Project ConFlex (PID2023-151880OB-C33), project DEMARSYS (PID2023-152771OB-I00) and Generalitat Valenciana *via* Prometeo Grant Q-Solutions (CIPROM/2021/078). A. F. G.-R. thanks ANID for the financial support through the FONDECYT Iniciación Project (Grant no. 11240161) and Vinculación Internacional Project (FOVI240255). J. R.-P. thanks the Ministry of Education, Youth and Sports of the Czech Republic for the support of large research infrastructures CEMNAT (project LM2023037). S.-Y. L. acknowledges support from the Basic Science Research Program through the National Research Foundation of Korea (NRF) funded by the Ministry of Education (RS-2025-25427101). The authors are very grateful to the "Serveis Centrals d'Instrumentació Científica (SCIC)" of the Universitat Jaume I.

References

1 H. Zhang, B. Zhang, X. Wang, L. Zou, J. You and S. Lin, Effective charge separation in photoelectrochemical water splitting: a review from advanced evaluation methods to materials design, *Sustain. Energy Fuels*, 2024, **8**(11), 2357–2382, DOI: 10.1039/d4se00390j.

2 A. E. Karaca and I. Dincer, Development of a new photoelectrochemical system for clean hydrogen production and a comparative environmental impact assessment with other production methods, *Chemosphere*, 2023, **337**, 139367, DOI: 10.1016/j.chemosphere.2023.139367.

3 M. Grätzel, Photoelectrochemical cells, *Nature*, 2001, **414**(6861), 338–344, DOI: 10.1038/35104607.

4 B. Klahr, S. Gimenez, O. Zandi, F. Fabregat-Santiago and T. Hamann, Competitive Photoelectrochemical Methanol and Water Oxidation with Hematite Electrodes, *ACS Appl. Mater. Interfaces*, 2015, **7**(14), 7653–7660, DOI: 10.1021/acsami.5b00440.

5 Z.-J. Li, E. Hofman, J. Li, A. H. Davis, C.-H. Tung, L.-Z. Wu and W. Zheng, Photoelectrochemically Active and Environmentally Stable CsPbBr3/TiO2 Core/Shell Nanocrystals, *Adv. Funct. Mater.*, 2018, **28**(1), 1704288, DOI: 10.1002/adfm.201704288.

6 A. A. Mamun, A. H. Chowdhury, A. Billah, J. Karim, A. O. Hussain, F. Rahman and M. A. Talukder, Advancing Transition Metal Oxide Photoelectrodes for Efficient Solar-Driven Hydrogen Generation: Strategies and Insights, *Adv. Energy Mater.*, 2025, **15**, 2501766, DOI: 10.1002/aenm.202501766.

7 Q. Wang, Z. Wang, N. Liao, S. Montilla-Verdú, M. Contreras, N. Guijarro and J. Luo, Tailoring the Surface Termination of BiVO4 Photoanodes Using Ammonium Metavanadate Enhances the Solar Water Oxidation Performance, *ACS Energy Lett.*, 2024, **9**(7), 3308–3315, DOI: 10.1021/acsenergylett.4c01240.

8 X. Zhu, N. Guijarro, Y. Liu, P. Schouwink, R. A. Wells, F. Le Formal, S. Sun, C. Gao and K. Sivula, Spinel Structural Disorder Influences Solar-Water-Splitting Performance of ZnFe2O4 Nanorod Photoanodes, *Adv. Mater.*, 2018, **30**(34), 1801612, DOI: 10.1002/adma.201801612.

9 J. H. Kim and J. S. Lee, Elaborately Modified BiVO4 Photoanodes for Solar Water Splitting, *Adv. Mater.*, 2019, **31**(20), 1806938, DOI: 10.1002/adma.201806938.

10 T.-Y. Kim, B. S. Kim, J. G. Oh, S. C. Park, J. Jang, T. W. Hamann, Y. S. Kang, J. H. Bang, S. Giménez and Y. S. Kang, Interfacial Engineering at Quantum Dot-Sensitized TiO2 Photoelectrodes for Ultrahigh Photocurrent Generation, *ACS Appl. Mater. Interfaces*, 2021, **13**(5), 6208–6218, DOI: 10.1021/acsami.0c19352.

11 Z. G. Schichtl, O. Q. Carvalho, J. Tan, S. S. Saund, D. Ghoshal, L. M. Wilder, M. K. Gish, A. C. Nielander, M. B. Stevens and A. L. Greenaway, Chemistry of Materials Underpinning Photoelectrochemical Solar Fuel Production, *Chem. Rev.*, 2025, **125**(10), 4768–4839, DOI: 10.1021/acs.chemrev.4c00258.

12 M. Volokh, G. Peng, J. Barrio and M. Shalom, Carbon Nitride Materials for Water Splitting Photoelectrochemical Cells, *Angew. Chem., Int. Ed.*, 2019, **58**(19), 6138–6151, DOI: 10.1002/anie.201806514.

13 S. Mondal, A. Tashakory, G. Mark, S. Barzilai, A. Pedersen, M. Volokh, J. Albero, H. García and M. Shalom, Enhanced activity and stability of polymeric carbon nitride photoanodes by yttrium incorporation, *EES Catal.*, 2025, **3**(4), 800–810, DOI: 10.1039/d5ey00064e.

14 C. Pulignani, C. A. Mesa, S. A. J. Hillman, T. Uekert, S. Giménez, J. R. Durrant and E. Reisner, Rational Design of Carbon Nitride Photoelectrodes with High Activity Toward Organic Oxidations, *Angew. Chem.*, 2022, **61**(50), e202211587, DOI: 10.1002/ange.202211587.

15 C. Nomellini, A. Polo, C. A. Mesa, E. Pastor, G. Marra, I. Grigioni, M. V. Dozzi, S. Giménez and E. Selli, Improved Photoelectrochemical Performance of WO3/BiVO4 Heterojunction Photoanodes via WO3 Nanostructuring, *ACS Appl. Mater. Interfaces*, 2023, **15**, 52436–52447, DOI: 10.1021/acsami.3c10869.

16 M. García-Tecedor, D. Cardenas-Morcoso, R. Fernández-Climent and S. Giménez, The Role of Underlayers and Overlayers in Thin Film BiVO4 Photoanodes for Solar Water Splitting, *Adv. Mater. Interfaces*, 2019, **6**(15), 1900299, DOI: 10.1002/admi.201900299.

17 H.-H. Cho, L. Yao, J.-H. Yum, Y. Liu, F. Boudoire, R. A. Wells, N. Guijarro, A. Sekar and K. Sivula, A semiconducting polymer bulk heterojunction photoanode for solar water oxidation, *Nat. Catal.*, 2021, **4**(5), 431–438, DOI: 10.1038/s41929-021-00617-x.

18 X. Wang, F. Wang, Y. Sang and H. Liu, Full-Spectrum Solar-Light-Activated Photocatalysts for Light–Chemical Energy Conversion, *Adv. Energy Mater.*, 2017, **7**(23), 1700473, DOI: 10.1002/aenm.201700473.

19 Q. Xu, L. Zhang, B. Cheng, J. Fan and J. Yu, S-Scheme Heterojunction Photocatalyst, *Chem*, 2020, **6**(7), 1543–1559, DOI: 10.1016/j.chempr.2020.06.010.

20 R. Tang, S. Zhou, Z. Zhang, R. Zheng and J. Huang, Engineering Nanostructure–Interface of Photoanode Materials Toward Photoelectrochemical Water Oxidation, *Adv. Mater.*, 2021, **33**(17), 2005389, DOI: 10.1002/adma.202005389.

21 X. Ning and G. Lu, Photocorrosion inhibition of CdS-based catalysts for photocatalytic overall water splitting, *Nanoscale*, 2020, **12**(3), 1213–1223, DOI: 10.1039/c9nr09183a.

22 L.-J. Guo, J.-W. Luo, T. He, S.-H. Wei and S.-S. Li, Photocorrosion-Limited Maximum Efficiency of Solar Photoelectrochemical Water Splitting, *Phys. Rev. Appl.*, 2018, **10**(6), 064059, DOI: 10.1103/PhysRevApplied.10.064059.

23 J. De Roo, M. Ibáñez, P. Geiregat, G. Nedelcu, W. Walravens, J. Maes, J. C. Martins, I. Van Driessche, M. V. Kovalenko and Z. Hens, Highly Dynamic Ligand Binding and Light Absorption Coefficient of Cesium Lead Bromide Perovskite Nanocrystals, *ACS Nano*, 2016, **10**(2), 2071–2081, DOI: 10.1021/acsnano.5b06295.

24 A. Dey, J. Ye, A. De, E. Debroye, S. K. Ha, E. Bladt, A. S. Kshirsagar, Z. Wang, J. Yin, Y. Wang, *et al.*, State of the Art and Prospects for Halide Perovskite Nanocrystals, *ACS Nano*, 2021, **15**(7), 10775–10981, DOI: 10.1021/acsnano.0c08903.

25 R. Grisorio, E. Fanizza, I. Allegretta, D. Altamura, M. Striccoli, R. Terzano, C. Giannini, V. Vergaro, G. Ciccarella, N. Margiotta, *et al.*, Insights into the role of the lead/surfactant ratio in the formation and passivation of cesium lead bromide perovskite nanocrystals, *Nanoscale*, 2020, **12**(2), 623–637, DOI: 10.1039/c9nr08079a.

26 R. Grisorio, D. Conelli, R. Giannelli, E. Fanizza, M. Striccoli, D. Altamura, C. Giannini, I. Allegretta, R. Terzano and G. P. Suranna, A new route for the shape differentiation of cesium lead bromide perovskite nanocrystals with near-unity photoluminescence quantum yield, *Nanoscale*, 2020, **12**(32), 17053–17063, DOI: 10.1039/d0nr04246c.

27 D. B. Straus and R. J. Cava, Tuning the Band Gap in the Halide Perovskite CsPbBr3 through Sr Substitution, *ACS Appl. Mater. Interfaces*, 2022, **14**(30), 34884–34890, DOI: 10.1021/acsami.2c09275.

28 A. F. Gualdrón-Reyes, D. F. Macias-Pinilla, S. Masi, C. Echeverría-Arrondo, S. Agouram, V. Muñoz-Sanjosé, J. Rodríguez-Pereira, J. M. Macak and I. Mora-Seró, Engineering Sr-doping for enabling long-term stable FAPb1−xSrxI3 quantum dots with 100% photoluminescence quantum yield, *J. Mater. Chem. C*, 2021, **9**(5), 1555–1566, DOI: 10.1039/d0tc04625f.

29 Q. Zhao, A. Hazarika, L. T. Schelhas, J. Liu, E. A. Gaulding, G. Li, M. Zhang, M. F. Toney, P. C. Sercel and J. M. Luther,

Size-Dependent Lattice Structure and Confinement Properties in CsPbI3 Perovskite Nanocrystals: Negative Surface Energy for Stabilization, *ACS Energy Lett.*, 2020, **5**(1), 238–247, DOI: 10.1021/acsenergylett.9b02395.

30 A. F. Gualdron-Reyes, J. Rodriguez-Pereira, E. Amado-Gonzalez, J. Rueda-P, R. Ospina, S. Masi, S. J. Yoon, J. Tirado, F. Jaramillo, S. Agourani, *et al.*, Unravelling the Photocatalytic Behavior of All-Inorganic Mixed Halide Perovskites: The Role of Surface Chemical States, *ACS Appl. Mater. Interfaces*, 2020, **12**(1), 914–924, DOI: 10.1021/acsami.9b19374.

31 D. Cardenas-Morcoso, A. F. Gualdrón-Reyes, A. B. Ferreira Vitoreti, M. García-Tecedor, S. J. Yoon, M. Solis de la Fuente, I. Mora-Seró and S. Gimenez, Photocatalytic and Photoelectrochemical Degradation of Organic Compounds with All-Inorganic Metal Halide Perovskite Quantum Dots, *J. Phys. Chem. Lett.*, 2019, **10**(3), 630–636, DOI: 10.1021/acs.jpclett.8b03849.

32 R. Fernández-Climent, A. F. Gualdrón-Reyes, M. García-Tecedor, C. A. Mesa, D. Cárdenas-Morcoso, L. Montañes, E. M. Barea, E. Mas-Marzá, B. Julián-López, I. Mora-Seró, *et al.*, Switchable All Inorganic Halide Perovskite Nanocrystalline Photoelectrodes for Solar-Driven Organic Transformations, *Sol. RRL*, 2021, **6**, 2100723, DOI: 10.1002/solr.202100723.

33 Q. Jan, A. A. Wani, S. Nabi, A. Y. Bhat, M. M. Bhat, P. P. Ingole and M. A. Bhat, AuNP Plasmon-boosted MAPbBr3 perovskite nanocrystals for enhanced photoelectrochemical hydrogen evolution reaction, *Fuel*, 2025, **398**, 135542, DOI: 10.1016/j.fuel.2025.135542.

34 T. H. Kim, K. Cho, S. H. Lee, J. H. Kang, H. B. Park, J. Park and Y.-H. Kim, Spin polarization in Fe-doped CsPbBr3 perovskite nanocrystals for enhancing photocatalytic CO2 reduction, *Chem. Eng. J.*, 2024, **492**, 152095, DOI: 10.1016/j.cej.2024.152095.

35 W. Zhang, J. Xiao, R. Gao, Z. Sun, H. Wang, W. Wu and A. Feng, Trace organic–inorganic hybrid lead halide perovskite nanocrystals as photocatalysts for PET-RAFT polymerization with high efficiency, *Eur. Polym. J.*, 2024, **215**, 113220, DOI: 10.1016/j.eurpolymj.2024.113220.

36 A. F. Gualdrón-Reyes, C. A. Mesa, S. Giménez and I. Mora-Seró, Application of Halide Perovskite Nanocrystals in Solar-Driven Photo(electro)Catalysis, *Sol. RRL*, 2022, **6**(7), 2200012, DOI: 10.1002/solr.202200012.

37 F. Fang, W. Chen, Y. Li, H. Liu, M. Mei, R. Zhang, J. Hao, M. Mikita, W. Cao, R. Pan, *et al.*, Employing Polar Solvent Controlled Ionization in Precursors for Synthesis of High-Quality Inorganic Perovskite Nanocrystals at Room Temperature, *Adv. Funct. Mater.*, 2018, **28**(10), 1706000, DOI: 10.1002/adfm.201706000.

38 D. Chen, K. Xu, M. Yang, J. Hu, R. Li, D. Huang, S. Liang, K. He, L. Yuan, S. Wang, *et al.*, Surface chemistry engineering enables polar solvent resistant and highly emissive perovskite nanocrystals for multifunctional applications, *Chem. Eng. J.*, 2023, **471**, 144848, DOI: 10.1016/j.cej.2023.144848.

39 L. Li, L. Gan and Z. Zhang, Encapsulation Strategy on All Inorganic Perovskites for Stable and Efficient Photoelectrocatalytic Water Splitting, *Adv. Mater. Interfaces*, 2021, **8**(13), 2100202, DOI: 10.1002/admi.202100202.

40 G.-Y. Qiao, D. Guan, S. Yuan, H. Rao, X. Chen, J.-A. Wang, J.-S. Qin, J.-J. Xu and J. Yu, Perovskite Quantum Dots Encapsulated in a Mesoporous Metal–Organic Framework as Synergistic Photocathode Materials, *J. Am. Chem. Soc.*, 2021, **143**(35), 14253–14260, DOI: 10.1021/jacs.1c05907.

41 R. Tang, L. Wang, Z. Zhang, W. Yang, H. Xu, A. Kheradmand, Y. Jiang, R. Zheng and J. Huang, Fabrication of MOFs' derivatives assisted perovskite nanocrystal on TiO2 photoanode for photoelectrochemical glycerol oxidation with simultaneous hydrogen production, *Appl. Catal., B*, 2021, **296**, 120382, DOI: 10.1016/j.apcatb.2021.120382.

42 Z. Zhu, M. Daboczi, M. Chen, Y. Xuan, X. Liu and S. Eslava, Ultrastable halide perovskite CsPbBr3 photoanodes achieved with electrocatalytic glassy-carbon and boron-doped diamond sheets, *Nat. Commun.*, 2024, **15**(1), 2791, DOI: 10.1038/s41467-024-47100-2.

43 M. Daboczi, J. Cui, F. Temerov and S. Eslava, Scalable All-Inorganic Halide Perovskite Photoanodes with >100 h Operational Stability Containing Earth-Abundant Materials, *Adv. Mater.*, 2023, **35**(45), 2304350, DOI: 10.1002/adma.202304350.

44 I. Poli, U. Hintermair, M. Regue, S. Kumar, E. V. Sackville, J. Baker, T. M. Watson, S. Eslava and P. J. Cameron, Graphite-protected CsPbBr3 perovskite photoanodes functionalised with water oxidation catalyst for oxygen evolution in water, *Nat. Commun.*, 2019, **10**(1), 2097, DOI: 10.1038/s41467-019-10124-0.

45 R. Keshavarzi, F. Hajisharifi, P. Golabi, R. Sheibani and A. Dabirian, Highly efficient and stable CsPbBr3 perovskite photoanodes based on inverse opal TiO2 layers in photoelectrochemical water splitting, *J. Mater. Chem. A*, 2025, **13**(35), 29172–29182, DOI: 10.1039/d5ta01376c.

46 M. Kazes, T. Udayabhaskararao, S. Dey and D. Oron, Effect of Surface Ligands in Perovskite Nanocrystals: Extending in and Reaching out, *Acc. Chem. Res.*, 2021, **54**(6), 1409–1418, DOI: 10.1021/acs.accounts.0c00712.

47 F. Krieg, P. C. Sercel, M. Burian, H. Andrusiv, M. I. Bodnarchuk, T. Stöferle, R. F. Mahrt, D. Naumenko, H. Amenitsch, G. Rainò, *et al.*, Monodisperse Long-Chain Sulfobetaine-Capped CsPbBr3 Nanocrystals and Their Superfluorescent Assemblies, *ACS Cent. Sci.*, 2020, **7**(1), 135–144, DOI: 10.1021/acscentsci.0c01153.

48 A. Stelmakh, M. Aebli, A. Baumketner and M. V. Kovalenko, On the Mechanism of Alkylammonium Ligands Binding to the Surface of CsPbBr3 Nanocrystals, *Chem. Mater.*, 2021, **33**(15), 5962–5973, DOI: 10.1021/acs.chemmater.1c01081.

49 X.-D. Wang, Y.-H. Huang, J.-F. Liao, Z.-F. Wei, W.-G. Li, Y.-F. Xu, H.-Y. Chen and D.-B. Kuang, Surface passivated halide perovskite single-crystal for efficient photoelectrochemical synthesis of dimethoxydihydrofuran, *Nat. Commun.*, 2021, **12**(1), 1202, DOI: 10.1038/s41467-021-21487-8.

50 P. Papagiorgis, M. Sergides, A. Manoli, M. Athanasiou, C. Bernasconi, F. Galatopoulos, A. Ioakeimidis, C. Nicolaides, E. Leontidis, T. Trypiniotis, *et al.*, The Impact of Ligand Removal on the Optoelectronic Properties of Inorganic and Hybrid Lead Halide Perovskite Nanocrystal Films, *Adv. Opt. Mater.*, 2023, **12**(3), 2301501, DOI: 10.1002/adom.202301501.

51 P. Uribe-Vegas, A. Villanueva-Antolí, C. Segura, F. Werlinger, K. R. Aliaga, R. Caprile, O. S. Trofymchuk, M. E. Flores, I. O. Osorio-Román, C. Echeverría-Arrondo, *et al.*, The Role of Alkylammonium Bromides on the Surface Passivation of Stable Alcohol-Dispersed CsPbX3 Nanocrystals and on the Stability Enhancement in Light-Emitting Applications, *Adv. Opt. Mater.*, 2024, **12**, 2401475, DOI: 10.1002/adom.202401475.

52 V. K. Ravi, R. A. Scheidt, J. DuBose and P. V. Kamat, Hierarchical Arrays of Cesium Lead Halide Perovskite Nanocrystals through Electrophoretic Deposition, *J. Am. Chem. Soc.*, 2018, **140**, 8887–8894, DOI: 10.1021/jacs.8b04803.

53 T. C. A. da Silva, C. Fernández-Saiz, R. S. Sánchez, A. F. Gualdrón-Reyes, I. Mora-Seró and B. Julián-López, A soft-chemistry route to prepare halide perovskite nanocrystals with tunable emission and high optical performance, *J. Sol-Gel Sci. Technol.*, 2023, **114**, 131–138, DOI: 10.1007/s10971-023-06171-1.

54 D. Baranov, G. Caputo, L. Goldoni, Z. Dang, R. Scarfiello, L. De Trizio, A. Portone, F. Fabbri, A. Camposeo, D. Pisignano, *et al.*, Transforming colloidal Cs4PbBr6 nanocrystals with poly(maleic anhydride-alt-1-octadecene) into stable CsPbBr3 perovskite emitters through intermediate heterostructures, *Chem. Sci.*, 2020, **11**(15), 3986–3995, DOI: 10.1039/d0sc00738b.

55 H. Kim, J. H. Park, K. Kim, D. Lee, M. H. Song and J. Park, Highly Emissive Blue Quantum Dots with Superior Thermal Stability via In Situ Surface Reconstruction of Mixed CsPbBr3–Cs4PbBr6 Nanocrystals, *Adv. Sci.*, 2021, **9**(5), 2104660, DOI: 10.1002/advs.202104660.

56 A. Dutta, S. K. Dutta, S. Das Adhikari and N. Pradhan, Tuning the Size of CsPbBr3 Nanocrystals: All at One Constant Temperature, *ACS Energy Lett.*, 2018, **3**(2), 329–334, DOI: 10.1021/acsenergylett.7b01226.

57 Y. Huang, W. Luan, M. Liu and L. Turyanska, DDAB-assisted synthesis of iodine-rich CsPbI3 perovskite nanocrystals with improved stability in multiple environments, *J. Mater. Chem. C*, 2020, **8**(7), 2381–2387, DOI: 10.1039/c9tc06566k.

58 D. A. Tatarinov, S. S. Anoshkin, I. A. Tsibizov, V. Sheremet, F. Isik, A. Y. Zhizhchenko, A. B. Cherepakhin, A. A. Kuchmizhak, A. P. Pushkarev, H. V. Demir, *et al.*, High-Quality CsPbBr3 Perovskite Films with Modal Gain above 10 000 cm−1 at Room Temperature, *Adv. Opt. Mater.*, 2023, **11**(7), 2202407, DOI: 10.1002/adom.202202407.

59 C. A. Aranda, A. O. Alvarez, V. S. Chivrony, C. Das, M. Rai and M. Saliba, Overcoming ionic migration in perovskite solar cells through alkali metals, *Joule*, 2024, **8**(1), 241–254, DOI: 10.1016/j.joule.2023.11.011.

60 V. Naresh, S. Singh, H. Soh, J. Lee and N. Lee, Dual-phase CsPbBr3–CsPb2Br5 perovskite scintillator for sensitive X-ray detection and imaging, *Mater. Today Nano*, 2023, **23**, 100364, DOI: 10.1016/j.mtnano.2023.100364.

61 Y.-H. Chen, J.-Q. Shen, X.-L. Chen, L. Tang, N. Zhang, J.-Y. Zhang and Z.-J. Liu, Modulating CsPbBr3 nanocrystals encapsulated in PCN-224(Zr) for boosting full-spectrum-driven CO2 reduction: S-scheme transfer, photothermal-synergistic effect, and DFT calculations, *Sustain. Energy Fuels*, 2023, **7**(23), 5499–5512, DOI: 10.1039/d3se01029e.

62 H. Wu, Y. Zhang, M. Lu, X. Zhang, C. Sun, T. Zhang, V. L. Colvin and W. W. Yu, Surface ligand modification of cesium lead bromide nanocrystals for improved light-emitting performance, *Nanoscale*, 2018, **10**(9), 4173–4178, DOI: 10.1039/c7nr09126e.

63 C. Zhang, L. Turyanska, H. Cao, L. Zhao, M. W. Fay, R. Temperton, J. O'Shea, N. R. Thomas, K. Wang, W. Luan, *et al.*, Hybrid light emitting diodes based on stable, high brightness all-inorganic CsPbI3 perovskite nanocrystals and InGaN, *Nanoscale*, 2019, **11**(28), 13450–13457, DOI: 10.1039/c9nr03707a.

64 A. F. Gualdrón-Reyes, R. Fernández-Climent, S. Masi, C. A. Mesa, C. Echeverría-Arrondo, F. Aiello, F. Balzano, G. Uccello-Barretta, J. Rodríguez-Pereira, S. Giménez, *et al.*, Efficient Ligand Passivation Enables Ultrastable CsPbX3 Perovskite Nanocrystals in Fully Alcohol Environments, *Adv. Opt. Mater.*, 2023, **11**, 2203096, DOI: 10.1002/adom.202203096.

65 F. J. Mancilla, S. F. Rojas, A. F. Gualdrón-Reyes, M. I. Carreño-Lizcano, L. J. Duarte and M. E. Niño-Gómez, Improving the photoelectrocatalytic performance of boron-modified TiO2/Ti sol–gel-based electrodes for glycerol oxidation under visible illumination, *RSC Adv.*, 2016, **6**(52), 46668–46677, DOI: 10.1039/c6ra02806c.

66 G. F. Samu, Á. Balog, F. De Angelis, D. Meggiolaro, P. V. Kamat and C. Janáky, Electrochemical Hole Injection Selectively Expels Iodide from Mixed Halide Perovskite Films, *J. Am. Chem. Soc.*, 2019, **141**(27), 10812–10820, DOI: 10.1021/jacs.9b04568.

67 S. Lee, H.-S. Bae and W. Choi, Selective Control and Characteristics of Water Oxidation and Dioxygen Reduction in Environmental Photo(electro)catalytic Systems, *Acc. Chem. Res.*, 2023, **56**(7), 867–877, DOI: 10.1021/acs.accounts.3c00002.

68 E. Kalamaras and P. Lianos, Current Doubling effect revisited: Current multiplication in a PhotoFuelCell, *J. Electroanal. Chem.*, 2015, **751**, 37–42, DOI: 10.1016/j.jelechem.2015.05.029.

69 W. Zhang, B. Huang, Y. Cui, L. Shen and S. Yan, Investigation of the mechanism of methanol electrooxidation: a potential-dependent DFT study, *RSC Adv.*, 2025, **15**(14), 11056–11064, DOI: 10.1039/d5ra01511a.

70 H. Wang, E. Harkou, A. Constantinou, S. M. Al-Salemc, G. Manos and J. Tang, From photocatalysis to photon–phonon co-driven catalysis for methanol reforming to hydrogen and valuable by-products, *Chem. Soc. Rev.*, 2025, **54**(5), 2188–2207, DOI: 10.1039/d4cs00551a.

